remote sensing

MDPI

Article

Sensitivity of Optical Satellites to Estimate Windthrow Tree-Mortality in a Central Amazon Forest

Luciano Emmert [1,*], Robinson Isaac Negrón-Juárez [2], Jeffrey Quintin Chambers [2], Joaquim dos Santos [1], Adriano José Nogueira Lima [1], Susan Trumbore [3] and Daniel Magnabosco Marra [3]

[1] Forest Management Laboratory, National Institute of Amazon Research, Manaus 69060-062, AM, Brazil
[2] Climate Sciences Department, Lawrence Berkeley National Laboratory, Berkeley, CA 94720, USA
[3] Biogeochemical Processes Department, Max Planck Institute for Biochemistry, 07745 Jena, Germany; dmarra@bgc-jena.mpg.de (D.M.M.)
* Correspondence: lucianoemmert@yahoo.com.br

Abstract: Windthrow (i.e., trees broken and uprooted by wind) is a major natural disturbance in Amazon forests. Images from medium-resolution optical satellites combined with extensive field data have allowed researchers to assess patterns of windthrow tree-mortality and to monitor forest recovery over decades of succession in different regions. Although satellites with high spatial-resolution have become available in the last decade, they have not yet been employed for the quantification of windthrow tree-mortality. Here, we address how increasing the spatial resolution of satellites affects plot-to-landscape estimates of windthrow tree-mortality. We combined forest inventory data with Landsat 8 (30 m pixel), Sentinel 2 (10 m), and WorldView 2 (2 m) imagery over an old-growth forest in the Central Amazon that was disturbed by a single windthrow event in November 2015. Remote sensing estimates of windthrow tree-mortality were produced from Spectral Mixture Analysis and evaluated with forest inventory data (i.e., ground true) by using Generalized Linear Models. Field measured windthrow tree-mortality (3 transects and 30 subplots) crossing the entire disturbance gradient was 26.9 ± 11.1% (mean ± 95% CI). Although the three satellites produced reliable and statistically similar estimates (from 26.5% to 30.3%, $p < 0.001$), Landsat 8 had the most accurate results and efficiently captured field-observed variations in windthrow tree-mortality across the entire gradient of disturbance (Sentinel 2 and WorldView 2 produced the second and third best results, respectively). As expected, mean-associated uncertainties decreased systematically with increasing spatial resolution (i.e., from Landsat 8 to Sentinel 2 and WorldView 2). However, the overall quality of model fits showed the opposite pattern. We suggest that this reflects the influence of a relatively minor disturbance, such as defoliation and crown damage, and the fast growth of natural regeneration, which were not measured in the field nor can be captured by coarser resolution imagery. Our results validate the reliability of Landsat imagery for assessing plot-to-landscape patterns of windthrow tree-mortality in dense and heterogeneous tropical forests. Satellites with high spatial resolution can improve estimates of windthrow severity by allowing the quantification of crown damage and mortality of lower canopy and understory trees. However, this requires the validation of remote sensing metrics using field data at compatible scales.

Keywords: blowdowns; crown damage; forest inventory; extreme wind gusts; natural disturbances; spatial resolution; Spectral Mixture Analysis

Citation: Emmert, L.; Negrón-Juárez, R.I.; Chambers, J.Q.; Santos, J.d.; Lima, A.J.N.; Trumbore, S.; Marra, D.M. Sensitivity of Optical Satellites to Estimate Windthrow Tree-Mortality in a Central Amazon Forest. *Remote Sens.* **2023**, *15*, 4027. https://doi.org/10.3390/rs15164027

Academic Editor: Jan Altman

Received: 19 May 2023
Revised: 29 July 2023
Accepted: 1 August 2023
Published: 14 August 2023

1. Introduction

Windthrows (i.e., trees snapped and uprooted by wind) are the major mechanism of tree mortality in the Amazon, and can influence forest structure, species composition, and carbon balance [1–4]. Windthrows are associated with extreme rainfall events, mostly produced by mesoscale convective systems [5]. Under climate change, the intensity and frequency of convective storms is predicted to increase [6,7]. Thus, accurately quantifying

the occurrence of windthrows and associated tree mortality can contribute to understanding their ecosystem effects, and to predict how forests will respond to altered disturbance regimes [8–11].

Optical satellite imagery with medium spatial resolution (from 10 m to 39.9 m pixel size) [12], such as Landsat, combined with field data has allowed researchers to assess patterns of tree damage and mortality, and to monitor forest recovery over decades of subsequent succession in different regions [13–15]. These studies demonstrated that windthrows affect a large portion of the Amazon and occur with a range of intensities and sizes. The Central and Northwestern Amazon regions concentrate the highest incidence of large-scale (>30 ha) events [13,16,17].

Landsat offers broad coverage of the Earth's surface and long-term imagery data [18–20], allowing for reliable estimates of windthrow tree mortality at the stand, landscape, and regional scales [13,14,17]. However, robust estimates of tree mortality depend on the compatibility between the spatial resolution of optical sensors and the grain size of targets [21,22]. For this reason, using Landsat to detect windthrows formed by clusters of less than ~6–8 dead trees is challenging [23]. Even for larger windthrows (>5 ha), Landsat assessments may underestimate tree mortality by not accurately capturing relatively lower levels of disturbance on the periphery of impacted patches or due to surviving trees and the relatively fast regrowth of the natural regeneration [13,24].

Obtaining reliable estimates of tree mortality using remote sensing is not a trivial task. The quality of such estimates is highly dependent on the target of interest (e.g., single or clustering dead-trees, [25,26]), the methods used to quantify windthrow severity [27], and the characteristics of the employed sensors (e.g., spatial, temporal, and spectral resolutions [21,28,29]). The spatial resolution of satellites has been treated as an important variable in this process as it can improve the detection capability of small and diffuse vegetation damage, and thus minimize the influence of spectral mixing [30]. Spectral mixing tends to dilute the spectral signature of tree damage and mortality with other elements within the pixels. This includes shadow, exposed soil, or surviving trees within a matrix of impacted forest [27,31]. High spatial resolution satellite data, such as QuickBird, IKONOS, GeoEye, and WorldView, are suitable for detecting small canopy gaps in dense tropical forests [32–36] and have been shown to be efficient, even for detecting individual tree mortality in the Amazon [25,26,34,37,38].

In addition to optical satellites, other approaches such as SAR (Synthetic-Aperture Radar [39,40]), LiDAR [41–43] and aerial photos [44] have been tested to estimate tree-mortality associated with windthrows. SAR offers data that are less dependent on weather effects and with spatial resolutions comparable to high- and medium-resolution satellites [45,46]. However, this technology has not yet been tested for the Amazon, and a study conducted in a temperate forest showed that windthrow detection was not reliable due to shading and overlap effects that are common in mountainous areas, as well as the polarization and distortions associated with the angle of incidence during image acquisition [46]. Although aerial photos, LiDAR, and high-resolution satellites provide high-quality data, they have relatively restricted spatial and temporal coverage, high costs, and variations in light conditions and angles of view. These aspects restrict the use of such imagery for assessing patterns of forest damage and recovery [47].

Previous studies have successfully related windthrow tree-mortality recorded in forest inventories to changes in reflectance by using Spectral Mixture Analysis (SMA) [27] of Landsat images [13,14,16]. These studies show a consistent correlation between field and remote sensing data. Recent advances in computational techniques using Machine Learning have enabled the automatic detection of windthrows in forests outside the Amazon using high spatial resolution satellite imagery [48–50]. These techniques could enhance future research results using high spatial resolution imagery [51–53].

Although optical satellites with high spatial resolution (pixel size $\leq$10 m) have become available for the Amazon in the last decade, they have not yet been applied for mapping windthrows and quantifying associated tree mortality. Therefore, how windthrow tree

mortality estimates obtained with high-resolution satellites will be related to ground truth (i.e., precision and accuracy) in dense tropical forests remains unexplored.

Here, we combined optical remote sensing with forest inventory data across a disturbance gradient created by a single windthrow event from 2015 to investigate how spatial resolution affects the accuracy and precision of tree mortality estimates in the Central Amazon. Our study provides a framework for future research that aims to assess the severity of natural disturbances through reliable estimates of tree mortality. We addressed the following questions: (i) How does spatial resolution affect estimates of windthrow tree-mortality? (ii) Which sensor (i.e., Landsat 8, Sentinel 2, and WorldView 2) produces the most reliable estimates of tree mortality across an extent gradient of windthrow severities?

2. Materials and Methods

2.1. Study Area and Sampling Design

This research was conducted in a remote old-growth forest located near Manaus, Brazil (2°53′41″S, 60°16′26″W). This forest was impacted by a convective storm that occurred in November 2015, which propagated destructive wind gusts and rain and caused widespread tree mortality across an area of ~70 hectares (Figure 1a–c).

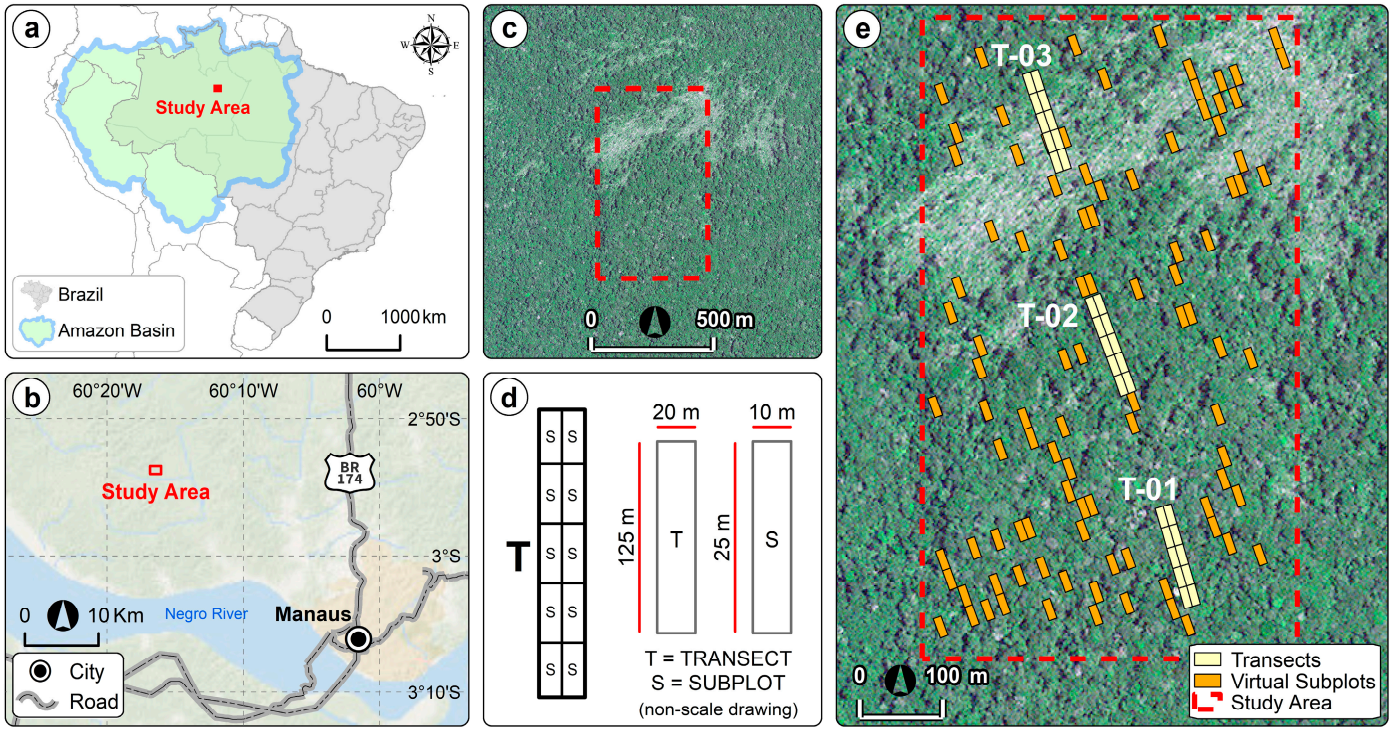

Figure 1. Windthrown forest located near Manaus, Central Amazon, Brazil (**a**,**b**), and inventory and virtual plots used to quantify tree mortality (**c**–**e**). Subfigures (**c**,**e**) are an RGB-composition from WorldView 2 image from 27 July 2016.

The windthrown area is covered by a forest transitioning from *terra-firme* (at the higher portions of the relief) to *campinarana*, such as described in adjacent areas [54–57]. *Terra-firme* is the most common upland forest type in the Amazon basin [58,59]. The lower portions of valleys (regionally known as *baixios*) can be temporally flooded by relatively small streams [60]. The *terra-firme* forests have a continuous canopy, dense understory, and high diversity of tree species [1,61–63]. *Campinaranas* are the predominant forest type that cover sandy soil patches with low nutrient content and poor drainage during the rainy season [64]. Compared to *terra-firme* forests, *campinaranas* have lower species richness and a distinct floristic composition due to their oligotrophic conditions [65]. In comparison to *terra-firme*, these forests usually have a decreased tree density, basal area, and biomass; shorter canopy; and are dominated by few tree species [55]. The transition between

terra-firme and *campinaranas* can aggregate species from both environments, and thus produce relatively high species diversity—for instance, having between 63 to 137 species in a single hectare [54]. Our study site is located in a remote area not affected by previous human or other large-scale natural disturbances during the last several decades.

The average annual temperature and precipitation in the region of Manaus (40 km from our study site) is 26.9 ± 0.17 °C and 2.231 ± 118 mm, respectively (mean ± 95% confidence interval for the period of 1970–2016, [2]). This region has an evident dry season from July to September, with monthly precipitation usually being less than 100 mm [13,16]. Soils on the plateaus have generally high clay content that transition to sandy soils in the lower portions [66,67]. In general, the soils have low fertility, low pH, high aluminum concentration, and low organic carbon content [60]. The local relief in our study region is undulating, including plateaus, slopes, and small valleys associated with perennial drainages [60,67].

To quantify windthrow tree-mortality in the field, we carried out a detailed forest inventory following a protocol built up from previous studies [1,2,13,14,23]. Following previous research conducted across different regions of the Amazon [1,2,4,23], we selected areas spanning the entire gradient of tree mortality within the affected forest, which were inspected in the field and through previous assessments that were performed by following well-established protocols [1,2]. Since this is a remote area for which no accessing infrastructure was available (e.g., roads and trails), our sampling also considered logistics limitations and the safety of our field crew. The forest inventory was performed over two campaigns conducted in December 2016 (~1 year after the windthrow) and April 2017 (~1.5 years after the windthrow). We established three 20 m × 125 m transects, subdivided into 10 subplots of 10 m × 25 m (250 m^2) (total of 30 subplots, hereafter referred to as field subplots). Our transects crossed the entire disturbance gradient, ranging from areas with little or no disturbance (i.e., unimpacted old-growth forest) to severely impacted forest with few or no surviving trees. In the field subplots, we recorded, identified, and measured the diameter at breast height (DBH) of all living trees with DBH ≥ 10 cm. Due to logistic and safety issues, we did not count dead trees in severely impacted areas. With this we also aimed to reduce random errors due to possible missing trees hidden below the large amount of coarse wood debris that is typical of windthrows (Figures S1–S4) [1,14]. Instead, we estimated the number of dead trees by subtracting the number of living/surviving trees recorded in each subplot from 15, which corresponds to mean tree density in adjacent old-growth forests (i.e., ~590 trees ha^{-1}, or 15 trees in 250 m^2, Table S1, [1,4,54–56,68–70]). The subplots with more than 15 live trees were considered as undisturbed (i.e., no associated windthrow tree-mortality).

2.2. Spectral Mixture Analysis and Remote Sensing Estimates of Windthrow Tree-Mortality

We used Landsat 8 and Sentinel 2 images acquired before and after the studied windthrow event (11 September 2015 and 27 July 2016, and 25 August 2015 and 30 July 2016, respectively). For the WorldView 2, we only used an image acquired after the event (27 July 2016). Landsat 8 and Sentinel 2 were downloaded from the Google Earth Engine platform (https://earthengine.google.com/, accessed on 25 April 2022) [71], and WorldView 2 was purchased from Digital Globe. We selected images with the minimum percent cloud cover, the closest pass dates to each other, and the greatest proximity between the acquisition date and the occurrence of the studied windthrow (Table S2).

We used Spectral Mixture Analysis (SMA) [72,73] and quantified the fractions of endmembers [27] following a well-known routine that was established in previous studies [9,13,14,16,23]. The endmembers contain specific spectral signatures of multiple elements that make up the forest surface and can be used to compute fraction images for different targets of interest [74,75]. We quantified the fraction of the following endmembers: green vegetation (GV, i.e., photosynthetically active vegetation), non-photosynthetic vegetation (NPV, i.e., dead vegetation), and shade (SHD) [27]. Endmembers were extracted and quantified using the software, ENVI 5.3 [27,76–79].

We used Landsat 8 and Sentinel 2 imagery with pixel values corrected for top-of-atmosphere (TOA) reflectance. For WorldView 2, a band-by-band radiometric correction factor was used to bring pixel values to the same range as Landsat 8 and Sentinel 2 [80]. As the evaluated satellites have different numbers of bands and respective spectral ranges, we obtained the spectral signatures of the focal endmembers by using the bands common to all of them. For Landsat 8 and Sentinel 2, we used the blue, green, red, NIR, and SWIR bands. Since WorldView 2 has a smaller spectral range, we used the blue, green, red, red edge, and NIR bands. The selected bands are sensitive to the physical, chemical, and anatomical characteristics of the leaves and trunks, thereby maximizing the distinction between GV and NPV [72,74,75].

We used the Purity Pixel Index spectral toolkit ([81], Figure S8) that relied on a well-established and reliable method that has been extensively used [1,14,16,17] to select the purest pixels from all images (e.g., areas where all trees were downed versus unaffected old-growth forest) to acquire the most accurate/representative endmembers of interest [27]. Finally, we conducted a SMA to compute fraction images of GV, NPV, and SHD [73]. Windthrows have a specific spectral signature for the NPV fraction, which originated from the deposition of large amounts of dead leaves and wood debris on the forest floor [82]. To ensure that the GV fraction represented forest patches not affected by the studied windthrow, we selected endmembers within the adjacent old-growth forest. The SHD endmember was selected from rivers in the vicinity of the impacted area.

The SHD endmember quantifies the effects of shading associated with the acquisition angle of images, canopy roughness, topography, and clouds [27,83]. Shading is highly related to the biophysical characteristics of trees and a major aspect contributing to variations in radiance and reflectance of canopies [74]. In tropical forests, shade can represent 30% of the canopy pixels and this effect can be observed in the red and NIR bands of medium- and high-resolution imagery [31]. In windthrown forests, a systematic reduction in the shadow fraction can be expected; however, the shadow fraction remains relatively high in areas that were less impacted and at the edge of gaps [23]. We conducted our analyses using the normalized GV and NPV fractions, for which the sum equals to 1 using the following equation:

$$\mathrm{NPV}_{\mathrm{norm}} = \frac{\mathrm{NPV}}{(\mathrm{GV} + \mathrm{NPV})} \quad (1)$$

where $\mathrm{NPV}_{\mathrm{norm}}$ is the normalized values of the endmembers ranging from 0 to 1 [27]. This implies that a reduction in one fraction leads to an increase in the other fraction by the same proportion [27] (Figure S10). The best images were selected according to [84], our field observations, and the spatial distribution of $\mathrm{NPV}_{\mathrm{norm}}$ values across the windthrow patches visible in the RGB compositions. We checked the histograms of the $\mathrm{NPV}_{\mathrm{norm}}$ images and selected those with more than 98% of the pixels with values between 0 and 1 [85]. We also used the residual error (RMS) from the SMA as a selection criterium (i.e., the lower the better) (Figure 2).

The differences between the $\mathrm{NPV}_{\mathrm{norm}}$ before (i.e., old-growth) and after disturbance (ΔNPV) provide a quantitative measure of windthrow tree-mortality [9,86]. The larger the ΔNPV values, the greater the windthrow tree-mortality [9,14,23]. For Landsat 8 and Sentinel 2, we calculated the ΔNPV fraction using the selected pair of images as described earlier (Table S6). In addition, we focused on images whose acquisition date was as close as possible to the windthrow date. We defined the probable date of occurrence based on the analysis of a time-series of Sentinel 2, which has a shorter revisiting time (~5 days) compared to Landsat 8 (~16 days).

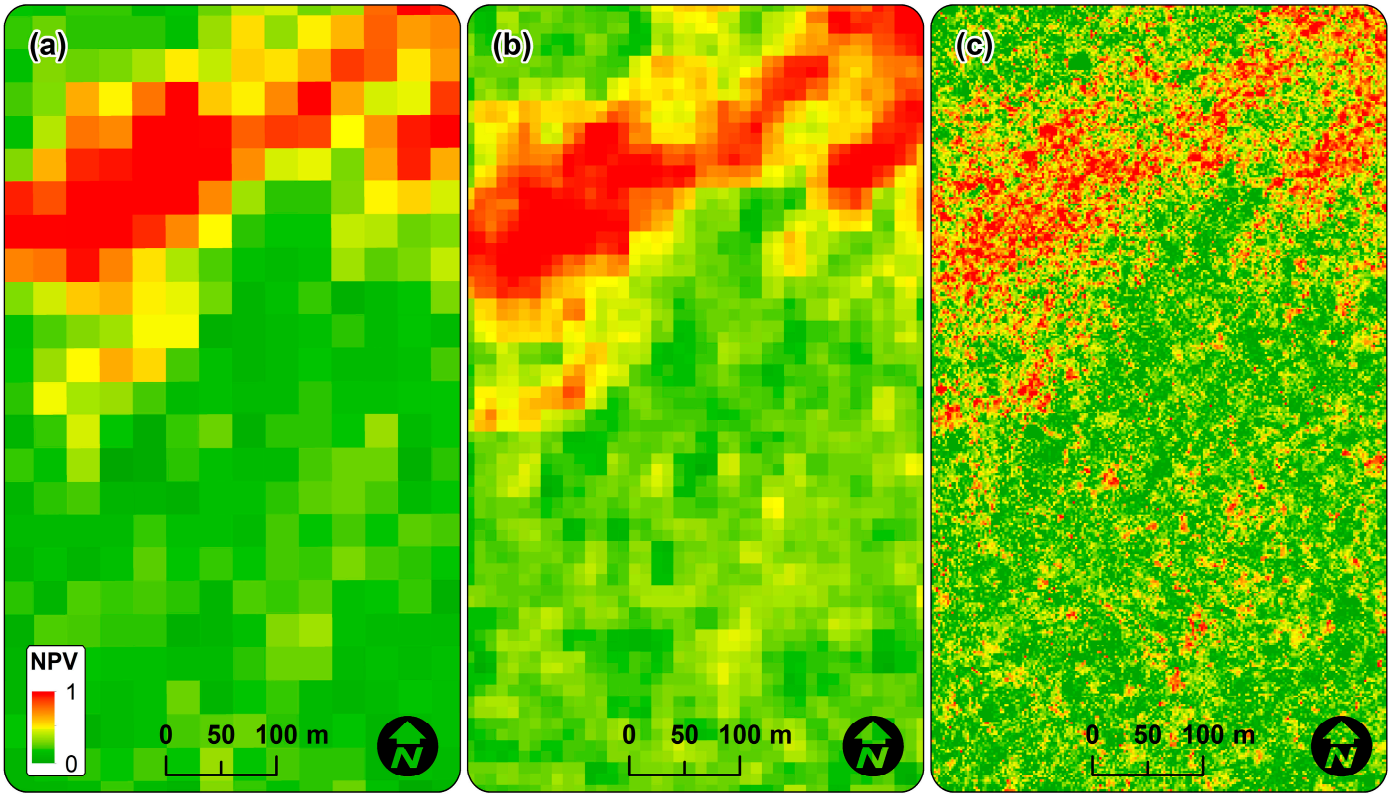

Figure 2. Cuts of selected NPV_{norm} images obtained from Spectral Mixture Analysis. (**a**) Landsat 8; (**b**) Sentinel 2; (**c**) WorldView 2.

This approach could not be implemented for WorldView 2, for which we had a single image after the windthrow. The NPV_{norm} and ΔNPV for Landsat 8 and Sentinel 2 varied with similar ranges and amplitudes (Figures S5 and S6, Tables S5 and S6). As supported by this pattern and the old-growth stage of forest surrounding the windthrown areas (i.e., no human or large-scale natural disturbances), comparison analyses were conducted for NPV_{norm} of the three satellites.

We calculated NPV_{norm} at subplot level (Table S3). For this, we converted the NPV_{norm} images in raster format to NPV_{norm} polygons in shapefile format using QGIS [87]. We further intersected the subplot shapefile polygon with the NPV_{norm} polygons for isolating all segments inside respective subplots. Thus, for each field subplot we obtained one or more segments of NPV_{norm}. We calculated the area of each NPV_{norm} polygon to obtain a weighted NPV value for each subplot [1,2,4] as:

$$NPV = \frac{NPV_{norm} * A}{250} \quad (2)$$

where NPV is the weighted value within each subplot, NPV_{norm} is the normalized value of each pixel, and A is the area of each pixel (m^2) that is fully or partially included in the respective subplot; 250 is equivalent to the area (m^2) of each subplot.

Apart from the 30 field subplots, we estimated windthrow tree mortality for 100 virtual subplots (10 m × 25 m; hereafter referred to as virtual subplots) that were randomly distributed across the disturbed forest (Figure 1d,e). These virtual subplots were used to evaluate the robustness of tree mortality estimates by the three satellites in adjacent areas containing a greater variation of windthrow severity (Figure 1e). The NPV weighted values for virtual subplots were obtained using the same method described for field subplots.

2.3. Remote Sensing Estimates of Windthrow Tree Mortality

We fitted a Generalized Linear Model (GLM) [88] relating NPV with field-measured windthrow tree-mortality (see Section 2.1). The GLMs were fitted for each satellite. We described the distribution of residuals using the binomial family, and used the *logit* link function, in which linear predictors must be reversed to the scale of the observations by means of an inverse function [88].

We used the field subplots only for model fitting, thus avoiding overfitting problems for the cases in which the validation was performed using the same subplots [89]. Virtual subplots were not used for validation/training; we focused on evaluating the performance of the models, and also assessed the Residual Deviance using Analysis of Variance (ANOVA). For each model we calculated the Akaike Information Criteria (AIC, [90]), Standard Error of the Estimates (S_{yx}), Root Mean Square Error (RMSE), Residual Standard Deviation (Sigma), and the Adjusted Coefficient of Determination (R^2) computed with the Kullback-Leibler divergence formula (R^2_{KL}, [91]). The R^2_{KL} is suitable for exponential family models (e.g., logit), which retains the informative properties of the fit due to the inclusion of regressors [91,92]. Unlike the linear model, which is based on the Ordinary Least Squares (OLS) approach, R^2 in these models does not represent the proportion of variability explained, because the binomial distribution does not have the same variability structure as the normal distribution used in simple linear regression [93]. For this reason, some methods for measuring the goodness-of-fit of GLM models, in particular for log-link families (e.g., binomial, exponential, gamma), have been constructed to express one more diagnostic measure of the nonlinear models. Among the available methods, the R^2_{KL} (Kullback's formula) provides a measure of the divergence between the distribution of observed and estimated values [91,92]. This measure can be used analogously to the R^2 for quantifying how much of the variation of field-measured tree mortality was captured by the fitted models [94]. The best model was the one with the lower Residual Deviance, AIC, S_{yx}, RMSE, Sigma, and higher R^2_{KL}.

We assessed the precision (i.e., minimum [Min], maximum [Max], median, and mean) and accuracy (i.e., standard deviation [SD], standard error [SE], and 95% confidence interval of the mean [hereafter referred to as 95% CI]) of remote estimates of tree mortality. For comparing our results with those reported for other Amazon regions [2,4], we also expressed windthrow tree-mortality as categories of severities: old-growth/undisturbed forest [$\leq$4% of windthrow tree mortality]; low windthrow severity [4% < windthrow tree mortality $\leq$ 20%]; moderate windthrow severity [20% < windthrow tree mortality $\leq$ 40%]; high windthrow severity [40% < windthrow tree mortality $\leq$ 60%]; and extreme windthrow severity [>60% of windthrow tree mortality]).

2.4. Statistical Analysis

To determine the most appropriate statistical tools for this study, we assessed the assumptions required for the use of parametric and non-parametric approaches [95]. We tested whether our measurements and estimates of windthrow tree mortality were normally and homogeneously distributed using the Shapiro-Wilk and Levene variance tests, respectively. As our data were not normally distributed and field subplots were nested in the transects, we further conducted a non-parametric approach. We further applied the Kruskal-Wallis test on medians [93] to assess possible differences between the distribution of estimated and measured values of windthrow tree mortality. Differences between field and remote sensing estimates were assessed using the Mann-Whitney post-hoc test, which allows for comparing paired data sets. Although the arithmetic mean is not a precise measure of central tendency for non-parametric data [93], we also reported weighted mean values of field-measured and remote-estimated tree mortality, as supported by the Central Limit Theorem [96]. We further analyzed differences among satellites using ANOVA, followed by the Tukey post-hoc test. Statistical analyses were conducted in the R 4.2.2 software [97] and based on a probability level of 95%.

3. Results

3.1. How Does Spatial Resolution Affect Satellite Estimates of Windthrow Tree-Mortality?

Across all field subplots (0.75 ha), we sampled 341 live and 121 dead trees. This is equivalent to 616 ± 13.3 trees ha^{-1} (455 ± 70.2 and 161 ± 63.7 live and dead trees ha^{-1}, respectively) (mean ± 95% CI). Live trees were distributed across 142 species, 86 genera, and 36 families. The mean windthrow tree-mortality measured in the field was 26.9 ± 11.1%, with a median of 13%, and minimum and maximum values of 0% and 93%, respectively (Table S3).

Variations in windthrow tree mortality were efficiently captured by three satellites evaluated in our study. Overall, the best agreement between field measurements and satellite estimates (i.e., lower Residual Deviance, AIC, S_{yx}, RMSE, Sigma, and higher R^2_{KL}) was achieved with Landsat 8, followed by Sentinel 2 and WorldView 2. This result indicates that increasing the spatial resolution (i.e., from Landsat 8 to Sentinel 2 and WorldView 2) implied a systematic loss of quality of fit of the models. Moreover, increasing the spatial resolution did not consistently modify the intercept and slope values of models. Surprisingly, all satellites showed minimum values of tree mortality ranging from ~9–11% (intercept) and a slope close to one (Table 1).

Table 1. Fitting summary of GLM models used to relate field with remote sensing estimates of windthrow tree-mortality in a Central Amazon forest, Brazil. AIC = Akaike Information Criteria; S_{yx} = standard error of the estimates; RMSE = root mean square error; Sigma = residual standard deviation; R^2_{KL} = Kullback-Leibler coefficient of determination.

Model	Residual Deviance	AIC	S_{yx}	RMSE	Sigma	R^2_{KL}	Coefficients	
							a (Intercept)	b (Slope)
Landsat 8	125.33	183.37	0.2096	0.194	2.116	0.4342	9.08	0.9837
Sentinel 2	136.51	194.55	0.2211	0.209	2.208	0.3837	11.21	0.9719
WorldView 2	150.01	208.05	0.2234	0.219	2.315	0.3237	10.61	0.9977

We found a strong and positive correlation between NPV_{norm} and field measurements of windthrow tree-mortality ($p < 0.001$, all, Figure 3). The mean and median of remote estimates were statistically similar for both field (F = 0.003 and $p = 0.99$ [mean test]; $X^2_{Kruskal\text{-}Wallis} = 3.23$ and p-value = 0.36 [median test]) and virtual subplots (F = 0.70 and $p = 0.49$ [mean test]; $X^2_{Kruskal\text{-}Wallis} = 1.58$ and p-value = 0.45 [median test])). Increasing the spatial resolution of images led to an overall decrease of model uncertainties (lower standard deviation, standard error, confidence interval, and interquartile interval). There was an increase in the range of estimated values in a narrower range of distribution across the disturbed landscape, which also resulted in systematic reductions of the interquartile ranges (Table 2).

The sensitivity of satellites also varied across the windthrow tree-mortality gradient. Landsat 8 and Sentinel 2 had a similar trend curve that differed from that of WorldView 2 (Figure 3a). Overall, increasing the spatial resolution systematically decreased the quality of tree mortality (Figure 3b). Windthrow tree-mortality obtained from Landsat 8 and Sentinel 2 had a more uniform residual distribution than that of WorldView 2, which indicates that the sensitivity of the former satellites was less susceptible to bias at the extremes of the severity gradient (Figure 3c). Increasing spatial resolution led to higher sensitivity for capturing diffuse tree mortality, possible reflecting crown, and minor damage. However, it also led to underestimated estimates of tree mortality in severely damaged areas (Figure 4).

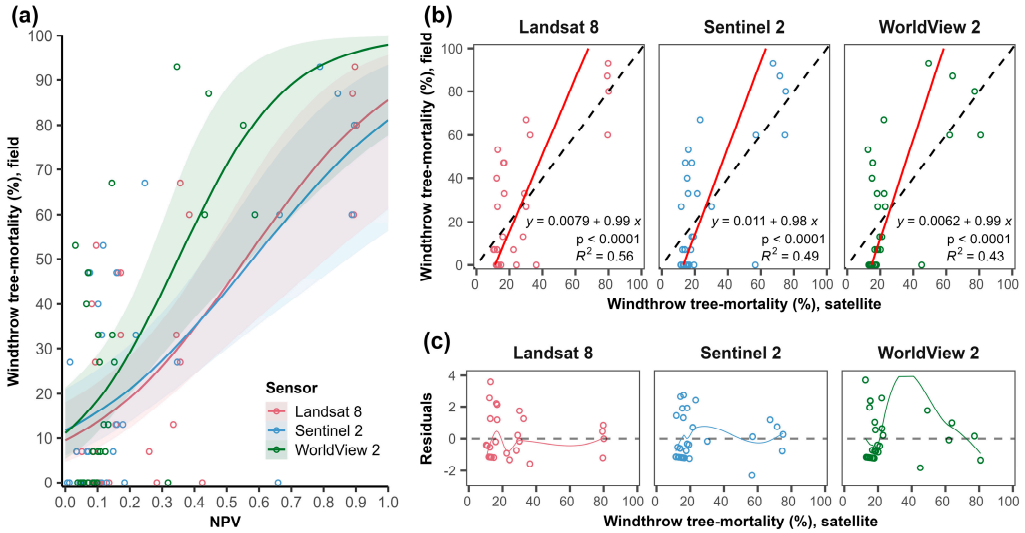

Figure 3. GLM models describing the relationship between windthrow tree-mortality measured in the field and estimated using remote sensing data. (**a**) Functions describing the relationship between NPV and windthrow tree-mortality (%) measured in the field; (**b**) Linear models describing the relationship between windthrow tree-mortality measured in the field and estimated using remote sensing. The black dotted and red lines are the 1:1 line (perfect linear relationship) and the actual relationship between observed and estimated values, respectively; (**c**) Symmetry of the distribution of residuals in relation to windthrow tree-mortality values estimated using remote sensing.

Table 2. Descriptive statistics of windthrow tree-mortality (%) measured in the field and estimated with remote sensing for a Central Amazon forest, Brazil. Min and Max-minimum and maximum values; Q1 and Q3-first and third median quartiles; Iqr-Interquartile range; SD-Standard Deviation; SE-Standard Error; CI-95% Confidence Interval. * Mean windthrow tree mortality similar among satellites.

Subplot Type	Measure	Min	Max	Median	Q1	Q3	Iqr	Mean	SD	SE	CI
Field	Field	0.0	93.0	13.0	0.0	47.0	47.0	26.9	29.7	5.4	11.1
	Landsat 8	10.3	80.1	16.1	12.8	29.8	17.0	26.5 *	22.5	4.1	8.4
	Sentinel 2	11.4	75.0	16.3	14.0	22.8	8.8	26.5 *	21.2	3.9	7.9
	WorldView 2	12.6	80.8	18.0	15.4	22.3	6.9	26.5 *	19.7	3.6	7.4
Virtual	Landsat 8	11.1	81.1	17.6	15.0	43.7	28.7	30.2	22.1	2.2	4.4
	Sentinel 2	11.7	80.2	19.5	16.2	40.9	24.7	30.3	19.5	1.9	3.9
	WorldView 2	13.1	92.0	21.2	16.8	32.2	15.4	27.4	16.1	1.6	3.2

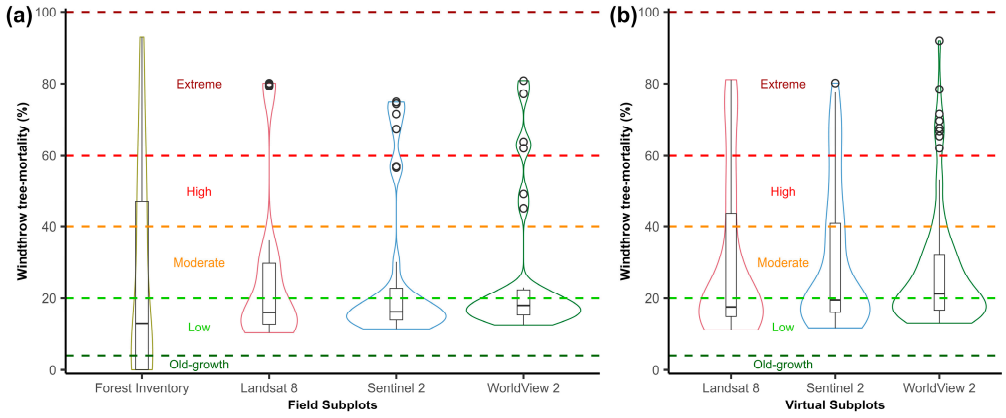

Figure 4. Distribution of windthrow tree-mortality (%) estimated from satellite data with varying spatial resolution (i.e., from 2 m to 30 m pixel). (**a**) Windthrow tree-mortality in field subplots; (**b**) Windthrow tree-mortality in virtual subplots. Hollow black circles are the outliers.

3.2. Which Sensor Produces the Most Reliable Estimates of Windthrow Tree-Mortality across an Extent Gradient of Windthrow Severity?

All satellites produced consistent estimates of windthrow tree-mortality from moderate to high disturbance severity (i.e., 25% to 42% of windthrow tree-mortality). Remote estimates overestimated field measurements by 5–10% from old-growth forest to moderate windthrow severity. From moderate to extreme windthrow severity, we found the opposite pattern—i.e., 10–15% underestimation (Figure 5a). Remote estimates of tree mortality for our virtual subplots covering a wider disturbance gradient were similar from low to moderate windthrow tree-mortality. From moderate to extreme windthrow tree-mortality, Landsat 8 and Sentinel 2 yielded comparable values, which were also different from those obtained from WorldView 2 (Figure 5b). Although with greater associated uncertainties at specific ranges of tree mortality (low to moderate and high to extreme severity), Landsat 8 and Sentinel 2 captured a relatively higher proportion of the existing variation of windthrow tree mortality over a wider disturbance gradient.

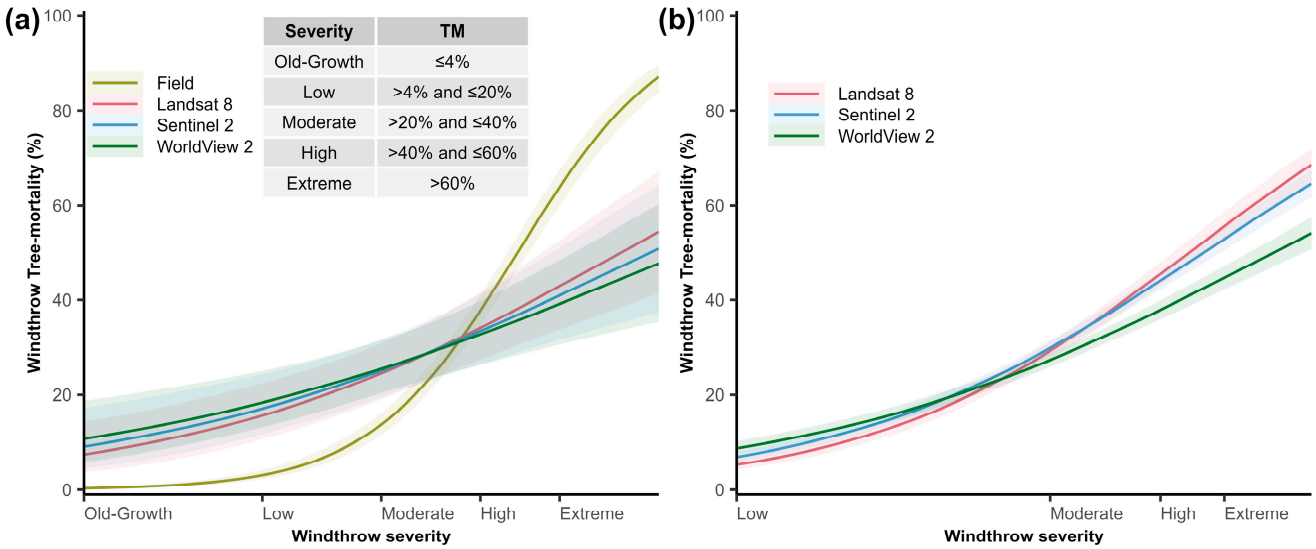

Figure 5. Windthrow tree-mortality measured in the field and estimated by remote sensing data for a Central Amazon forest, Brazil. (**a**) Windthrow tree-mortality in field subplots; (**b**) Windthrow-tree mortality in virtual subplots. In (**a**,**b**), we modeled remote estimates of tree mortality as a function of field measurements using GLMs. The gray-shaded areas in (**a**,**b**) indicate the 95% confidence interval. Field = Windthrow tree-mortality measured in the field; TM = Windthrow tree-mortality.

4. Discussion

4.1. Relating Satellite Data and Field Data

Systematic increase of spatial resolution implied changes on the sensitivity of different satellites to capture windthrow tree-mortality at the extremes of the disturbance gradient (i.e., low and severe mortality) (Table 2). In windthrown areas there is an abrupt reduction of GV followed by a consequent increase of NPV. Nonetheless, the NPV signal can be lost in less than a year due to the fast growth of pioneer species and survivor saplings and seedlings originally suppressed at the understory of the forest [1,14,23]. As supported by our data, the loss of the NPV signal might be critical for medium to high spatial resolution imagery with relatively small pixel sizes, which are more likely to be influenced by the fast emergence of photosynthetic/green vegetation (GV) [27] (Figure S10).

The convective storm that impacted our study region occurred about eight months (November/2015) prior to the acquisition of all satellite imagery (July/2016). Therefore, our NPV-fraction images may already contain some GV sign of the regenerating forest. This was evidenced by the relatively high reflectance values in the NIR and red edge bands (wavelength ~0.83 μm), which indicate a relatively high content of GV (i.e., photosynthetically active vegetation) [27,75] mixed with NPV (i.e., dead vegetation, wood debris)

(Figure S9). Systematic reductions of spectral mixing with increasing spatial resolution (i.e., from Landsat 8 to Sentinel 2 and further WorldView 2) may be related to specific admixture levels of GV. Although understory trees were not recorded in this study, our data support previous research indicating that high NPV values related to the dead vegetation tend to be rapidly diluted due to the fast natural regeneration (Figure S10).

The detection of tree damage and mortality using satellite data can be affected by several factors, such as canopy heterogeneity, understory density, angle-of-view/illumination, and shadow effects [74,78,98]. Overall, gains in spatial resolution improve the detection accuracy of detecting treefall gaps [33,34,37,42,99] as the spectral information tend to be highly influenced by geometric features of relatively small targets [32]. However, the number of pixels needed to capture the physical properties of the surfaces associated with large-scale windthrows is highly determined by the spectral resolution of imagery [100]. Since the mean reflectance of a given area is strongly influenced by the material with the highest reflectance values [74], the lower the spatial resolution of the sensor (i.e., the larger pixel size), the greater the mixture of signals produced by surfaces with relatively high reflectance. Smaller pixels can reduce these effects [78], which is supported by the higher sensitivity of WorldView 2 to capture diffuse tree mortality in less-disturbed areas and at edges of highly disturbed forest patches. WorldView 2 also produced higher tree mortality estimates than Landsat 8 and Sentinel 2 at low and moderate windthrow severity (4% < windthrow tree-mortality $\leq$ 40%). Given the relatively large diameter and area (mean of ~35 m^2, [101,102]) of canopy trees in our study region, this result suggests that WorldView 2 (4 m^2 pixel area) can potentially capture vegetation damage smaller than that measured in the field (i.e., individual tree-mortality). The intercepts for tree mortality varied from 9–11%, indicating that all satellites overestimated field values (Table 1). The variation of intercepts (Figure 3a)may also be related to scaling mismatches between field and imagery data and fine-scale variations of environmental attributes beyond the scope of this study. Furthermore, our models indicate that uncertainties associated with remote estimates of windthrow tree-mortality are larger at the extremes of the disturbance gradient (Figure 3b). R^2 values indicate that our models captured between 43% and 56% of the variation in field-measured mortality. We believe these values are robust given the variation of disturbance intensity typical of windthrown forests [1,2,4] and the time gap between the studied event and the acquisition date of employed images. Estimated tree-mortality was accurate (i.e., similar to the ground truth) across an extent range of windthrow severity (25–42%, moderate to high severity). As previously reported, these severities accounted for decadal changes in floristic composition [1,62,103], biomass stock and balance [2,4], organic soil carbon stocks [104], and insect diversity [105,106] in other Central and Northwestern Amazon forests affected by windthrows. Future investigations are needed to improve the remote detection of smaller canopy disturbances across local-to-regional variations in topography, climate, soils, and forest attributes [42–44,107].

High-resolution remote sensing models (HR-models) assume that elements are larger than image pixels; low-resolution models (LR-models) assume the opposite [108]. This means that the spatial arrangement of varying elements within an image can be detected directly in HR-models because individual elements can be individualized. This is usually not achieved with LR-models [21,108]. As predicted from our best model (Landsat 8), areas of forest that experienced high severity windthrow lost $\geq$ 50% of live trees. While a similar estimate of tree mortality can be attributed to two independent areas, they can have contrasting disturbance gradients given by the spatial distribution of damaged/dead trees (i.e., contiguous or diffuse) across impacted areas (Figure 3a).

In windthrows, the process of detecting and estimating tree mortality will transit between HR- and LR-models, depending on the level of disturbance severity and the size of pixels. For example, in a highly impacted area (e.g., assuming 50% dead trees and 50% live trees) inside one Landsat 30 m $\times$ 30 m pixel, the spatial autocorrelation among the trees is not detected because tree crowns and trunks are, in general, smaller than the pixel size. In this case, an unique reflectance value (i.e., single pixel) shall represent the

different targets (live and dead trees). The resulting measurement is highly influenced by the objects with high reflectance [75,100]. However, in HR-models, the same area is represented by several pixels (e.g., 2 m × 2 m pixel of WorldView 2). In this case, the spatial arrangement of the vegetation becomes relevant because trees are larger than the pixels, which tend to resemble their neighbors because they are likely to capture the signature of the same homogeneous target [27]. In HR-models, the varying information captured by several pixels will represent the entire set of live and dead trees. [21]. Depending on the size and severity of the windthrow in relation to the pixel size, HR- and LR-models will have different relationships between the number of dead trees in the field and the spectral/spatial information extracted at pixel level. Our results support that the more pixels within the subplots, the more detail on the spectral variability across the disturbed forest. However, tree damage (e.g., defoliation, broken branches, and partial loss of crown) should also be quantified in future forest inventories to maximize the potential of existing sensors with higher spatial-resolution than those we employed here (e.g., Planet Scope [109], Ikonos [110] and QuickBird [111]).

A precise match between field and remote sensing data also improves landscape estimates of tree mortality. In our study, pixels outside/inside observational subplots may have been incorrectly accounted for. Our plots were georeferenced with a navigation GPS (Garmin 64 CSx), which has a nominal spatial resolution usually >5 m. This effect was likely more relevant for WorldView 2. Geolocation errors for Landsat 8 are at the order of 30 m within the United States, and 50 m globally [112]. For Sentinel 2 and WorldView 2, global errors are at the order of 12.5 m [113,114] and 3.5 m [115], respectively. However, previous studies using the same plot size indicated a high correspondence between ground truth and the NPV signal obtained with Landsat [1,2].

As previously demonstrated, ΔNPV is highly correlated with windthrow tree mortality [1,2,23]. As supported by our results (Figure S5, Table S5), using NPV_{norm} for quantifying windthrow tree-mortality also produced robust and unbiased estimates. Nonetheless, the nature of such a relationship can be affected by variations in forest deciduousness and disturbance history (e.g., fragmented forests with larger proportion of edges or those submitted to multiple disturbances). Ideally, imagery covering the target forest should be available for pre- and post-disturbance conditions, and with the shortest possible time-interval between scenes.

4.2. Trade-Off between Precision and Accuracy of Satellite Estimates

By increasing spatial resolution and, consequently, the number of pixels representing a given target, we observed a systematic reduction of uncertainties (SD, SE, and CI) associated with our estimates of windthrow tree-mortality (Table 2). However, reductions in uncertainty were followed by systematic reductions in the quality of model fits, mostly due to large errors at the extremes of the disturbance gradient (i.e., low and extreme windthrow severity). This pattern suggests a trade-off between precision and accuracy [116]. In this case, precision indicates the reduction of uncertainty around the mean estimates, and accuracy indicates the closeness of the estimates in relation to the ground truth. In our study, all satellites delivered tree mortality estimates closer to the ground truth over a wide range of disturbance (from moderate to high windthrow severity). Future studies may extend and replicate our methods in regions with different forest attributes and environmental conditions.

Although we equalized TOA values prior to comparing images, each satellite has a different setup of imaging angles (Nadir) and spectral resolution. The Nadir angle may affect the detection of targets with irregular surfaces [74,98], such as in windthrown forests with high amounts of woody debris, survivor and new trees [1]. Large angles can imply obscuration of images and consequent distortion of geometric and spectral features of targets [111,117–119]. Landsat 8 images are acquired under Nadir ~0°, while Sentinel 2 and WorldView 2 have off-Nadir angles (~10.4° and ~20°, respectively). These differences may have reduced the quality of the NPV signal from Sentinel 2, and especially WorldView 2, in

relation to that obtained with Landsat 8. This may be critical in relatively small gaps or at the edge of highly impacted areas, where insolation is generally lower and the crown of given trees can promote strong shading effects on their neighbors [31,120,121]. To mitigate problems related to this issue, we normalized the fractions for GV and NPV without shade. This procedure ensures that the shadow fraction is filled by equal proportions of GV and NPV within the pixel [27]. Distortions due to the technical attributes of the different satellites were not the objective of the study, but we believe that these effects would not change the overall patterns we report. Apart from being usually acquired from off-Nadir angles due to acquisition costs or mission priorities, commercial high-resolution imagery, such as WorldView 2, can be costly and restricted to small areas [111]. These aspects limit the application of these for mapping windthrows and monitoring forest recovery across large regions and over time.

Indeed, our results show that spatial resolution alone does not provide sufficient evidence for the mismatch between field and remote data. Downgrading the spatial resolution of Sentinel 2 and WorldView 2 to that of Landsat 8 changes the relative weight of the NPV and GV fractions (i.e., reduction and increase of NPV and GV values, respectively) (Figure S11). This pattern indicates that spatial resolution has a direct effect on the sensitivity to detect windthrow tree-mortality, as well as to distinguish rapid post-disturbance regeneration. This has a direct effect on estimated values of windthrow severity at subplot level. Although higher spatial resolution has the potential to increase the sensitivity to detect crown damage and branch fall [44], it does not seem to have the potential to strongly improve stand-to-landscape estimates of windthrow tree-mortality. The accurate and precise estimates we achieved with Landsat 8 may also be partially related to its large pixel size (900 m^2) as in comparison to subplots (250 m^2).

Landsat 8 and Sentinel 2 have broad spectral resolutions and spectral bands that span from the visible to the shortwave infrared (0.43–2.2 µm) [122,123]. Meanwhile, WorldView 2 has a spectrum restricted to the visible and near infrared (0.4–1.04 µm) [115]. Different terrain materials mimicking the spectrum of others are common in dense forests, and the use of more channels (i.e., bands) is a general recommendation for extracting more suitable endmembers [27]. Thus, the lower spectral resolution of WorldView 2 may affect the process of selecting endmembers, and thus the overall quality of the Spectral Mixture Analysis.

The characteristics of the satellites we evaluated make them appropriate for specific conditions. While Landsat 8 and Sentinel 2 are freely available and cover the entire planet, WorldView 2 has high costs and covers only specific or by-demand regions. WorldView 2 has a 1.1-day revisiting time [115]; Sentinel 2 has a 5-day time [124], and Landsat 8 has a 16-day time [122]. Shorter revisiting time increases the chances of acquiring scenes shortly before and after the occurrence of windthrows. This aspect is essential to mitigate the contamination of NPV images due to fast natural regeneration. The high cloud cover in the Amazon [125] also limits the availability of images, and shorter revisit intervals can help overcome this limitation.

Landsat has a longer-term collection of images than Sentinel 2 or WorldView 2 [126], which makes it suitable for landscape-scale studies aiming at mapping windthrows and monitoring forest recovery over time [2,4]. However, Landsat may be inaccurate for quantifying and describing disturbances created by clusters of less than 6–8 fallen trees [23]. While restricted for the last 8 years, Sentinel 2 is a promising alternative for stand and landscape assessments of the extent and severity of forest disturbances at the individual-tree level. As Sentinel 2 produces estimates with overall low uncertainties, it may also perform better for quantifying diffuse tree mortality. Due to its continuity over the years [124], Sentinel 2 may soon allow for concealing longer-term analyses with high precision.

WorldView 2 estimates had lower associated uncertainties and were more accurate in areas with <20% tree mortality. However, the relatively small collection of images reduces the potential of using WorldView 2 for monitoring disturbance dynamics and forest recovery. The recently launched Planet NICFI initiative [109,127] conceals high

resolution (3–5 m pixel) multispectral imagery with a revisiting interval of less than four days for most of the Amazon basin [128]. This offers a new possibility for quantifying and upscaling major mechanisms of tree damage and mortality regulating forest dynamics and functioning.

5. Conclusions

Increasing the spatial resolution of satellite images reduced the uncertainty of estimates of windthrow tree-mortality but did not improve their accuracy. Compared to WorldView 2 and Sentinel 2, Landsat 8 provided more reliable estimates that reflected our field measurements at the individual tree-level. These results highlight the feasibility of Landsat 8 for mapping windthrows and monitoring forest recovery in the Amazon. To fully benefit from high-resolution images, field surveys used for model calibration should account for individual tree-damage (e.g., defoliation, crown breakage, and branch fall). However, high spatial resolution satellite imagery are expensive and restricted to small areas and time periods, which limits their application for large-scale and long-term assessments of mortality and recovery. Future studies applying high spatial resolution imagery could focus on overcoming the limitations of coarser sensors in detecting small clusters of dead trees and quantifying individual tree-damage. This will improve current knowledge on mechanisms and rates of tree mortality, as well as on associated processes regulating forest dynamics and carbon balance in Amazon forests.

Supplementary Materials: The following are available online at https://www.mdpi.com/article/10.3390/rs15164027/s1, Figure S1. General aspect of the studied windthrown forest, Figure S2. Delimitation of the accessing trails for conducting the forest inventory, Figure S3. Delimitation of the central tracks of the forest inventory plots, Figure S4. General aspect of fallen trees and piled debris in the studied area, Figure S5. GLM models describing the relationship between windthrow tree-mortality measured in the field and estimated using remote sensing data (ΔNPV), Figure S6. Distribution of windthrow tree-mortality (%) estimated with ΔNPV calculated for Landsat 8 and Sentinel 2, Figure S7. Windthrow tree-mortality measured in the field and estimated using ΔNPV calculated for Landsat 8 and Sentinel 2, Figure S8. Analysis routine for selecting endmembers used in Spectral Mixture Analysis and modeling, Figure S9. Spectral signature of the selected endmembers calculated for (a) Landsat 8, (b) Sentinel 2, and (c) WorldView 2, Figure S10. Distribution of NPV values estimated from satellite data with varying spatial resolution (i.e., from 2 m to 30 m pixel), Figure S11. Distribution of NPV values calculated from satellites with varying spatial resolution (from 2 m to 30 m pixel), Table S1. Reference data of tree density in Terra Firme/Campinarana forest in Central Amazon, Table S2. Satellite image collection and specifications, Table S3. Forest inventory and satellite estimates for the field subplots, Table S4. Fitting summary of GLM models used to relate field with remote sensing estimates of windthrow tree-mortality using ΔNPV for Landsat 8 and Sentinel 2 in a Central Amazon forest, Brazil, Table S5. Descriptive statistics for windthrow tree-mortality (%) measured in the field and from ΔNPV values calculated for Landsat 8 and Sentinel 2 for a Central Amazon forest, Brazil, Table S6. Forest inventory and satellite estimates of windthrow tree-mortality using ΔNPV values calculated for Landsat 8 and Sentinel 2 at the subplot level.

Author Contributions: L.E., R.I.N.-J. and D.M.M. planned and designed the research; R.I.N.-J. and D.M.M. collected field data; L.E. carried data analyzes with support from R.I.N.-J., J.d.S., A.J.N.L., J.Q.C., S.T. and D.M.M.; L.E. and D.M.M. wrote the manuscript with the support from all authors. All authors have read and agreed to the published version of the manuscript.

Funding: This research is part of the INVENTA (Interação Vento-Árvore na Amazônia), and the ATTO projects funded by the German Federal Ministry of Education and Research (BMBF contracts no. 01LB1001A and no. 01LK1602A), the Brazilian Ministry of Science, Technology, and Innovation (MCTI/FINEP contract no. 01.11.01248.00), and the Max Planck Society (MPG). L.E. was funded by the Amazonas State Research Support Foundation (FAPEAM) (PhD grant no. 41640.UNI739.1607.28032019-65939) and supported by the Instituto Nacional de Ciência e Tecnologia (INCT) Madeiras da Amazônia. R.I.N.-J and J.Q.C. were supported by the Office of Science, Office of Biological and Environmental Research of the US Department of Energy, Agreement grant DE-AC02-05CH11231, Next Generation Ecosystem Experiments-Tropics (NGEE-Tropics).

Data Availability Statement: The data presented in this study are available on request from the corresponding authors.

Acknowledgments: We thank Carlos Henrique de Sousa Celes and Raquel Fernandes Araujo for their support during the first field survey. We thank Rodrigo Geroni Nascimento, Walmes Zeviani and Maíra Conde for their support with statistical analysis, and Fabiano Emmert for his support with image processing and GIS analysis.

Conflicts of Interest: The authors declare no conflict of interest. The funders had no role in the design of the study; in the collection, analyses, or interpretation of data; in the writing of the manuscript, or in the decision to publish the results.

References

1. Marra, D.M.; Chambers, J.Q.; Higuchi, N.; Trumbore, S.E.; Ribeiro, G.H.P.M.; Dos Santos, J.; Negrón-Juárez, R.I.; Reu, B.; Wirth, C. Large-Scale Wind Disturbances Promote Tree Diversity in a Central Amazon Forest. *PLoS ONE* **2014**, *9*, e103711. [CrossRef]
2. Magnabosco Marra, D.; Trumbore, S.E.; Higuchi, N.; Ribeiro, G.H.P.M.P.M.; Negrón-Juárez, R.I.; Holzwarth, F.; Rifai, S.W.; dos Santos, J.; Lima, A.J.N.N.; Kinupp, V.F.; et al. Windthrows Control Biomass Patterns and Functional Composition of Amazon Forests. *Glob. Chang. Biol.* **2018**, *24*, 5867–5881. [CrossRef]
3. Rifai, S.W.; Urquiza Muñoz, J.D.; Negrón-Juárez, R.I.; Ramírez Arévalo, F.R.; Tello-Espinoza, R.; Vanderwel, M.C.; Lichstein, J.W.; Chambers, J.Q.; Bohlman, S.A. Landscape-Scale Consequences of Differential Tree Mortality from Catastrophic Wind Disturbance in the Amazon. *Ecol. Appl.* **2016**, *26*, 2225–2237. [CrossRef]
4. Urquiza Muñoz, J.D.; Magnabosco Marra, D.; Negrón-Juarez, R.I.; Tello-Espinoza, R.; Alegría-Muñoz, W.; Pacheco-Gómez, T.; Rifai, S.W.; Chambers, J.Q.; Jenkins, H.S.; Brenning, A.; et al. Recovery of Forest Structure Following Large-Scale Windthrows in the Northwestern Amazon. *Forests* **2021**, *12*, 667. [CrossRef]
5. Rehbein, A.; Ambrizzi, T.; Mechoso, C.R. Mesoscale Convective Systems over the Amazon Basin. Part I: Climatological Aspects. *Int. J. Clim.* **2018**, *38*, 215–229. [CrossRef]
6. IPCC. *Climate Change 2021: The Physical Science Basis. Contribution of Working Group I to the Sixth Assessment Report of the Intergovernmental Panel on Climate Change*; Masson-Delmotte, V., Zhai, P., Pirani, A., Connors, S.L., Péan, C., Berger, S., Caud, N., Chen, Y., Eds.; IPCC: Geneva, Switzerland, 2021.
7. Feng, Y.; Negrón-Juárez, R.I.; Romps, D.M.; Chambers, J.Q. Amazon Windthrow Disturbances Are Likely to Increase with Storm Frequency under Global Warming. *Nat. Commun.* **2023**, *14*, 101. [CrossRef]
8. Aleixo, I.; Norris, D.; Hemerik, L.; Barbosa, A.; Prata, E.; Costa, F.; Poorter, L. Amazonian Rainforest Tree Mortality Driven by Climate and Functional Traits. *Nat. Clim. Chang.* **2019**, *9*, 384–388. [CrossRef]
9. Chambers, J.Q.; Negron-Juarez, R.I.; Marra, D.M.; Di Vittorio, A.; Tews, J.; Roberts, D.; Ribeiro, G.H.P.M.; Trumbore, S.E.; Higuchi, N. The Steady-State Mosaic of Disturbance and Succession across an Old-Growth Central Amazon Forest Landscape. *Proc. Natl. Acad. Sci. USA* **2013**, *110*, 3949–3954. [CrossRef]
10. Esquivel-Muelbert, A.; Phillips, O.L.; Brienen, R.J.W.; Fauset, S.; Sullivan, M.J.P.; Baker, T.R.; Chao, K.J.; Feldpausch, T.R.; Gloor, E.; Higuchi, N.; et al. Tree Mode of Death and Mortality Risk Factors across Amazon Forests. *Nat. Commun.* **2020**, *11*, 5515. [CrossRef]
11. Gora, E.M.; Esquivel-Muelbert, A. Implications of Size-Dependent Tree Mortality for Tropical Forest Carbon Dynamics. *Nat. Plants* **2021**, *7*, 384–391. [CrossRef]
12. Belward, A.S.; Skøien, J.O. Who Launched What, When and Why; Trends in Global Land-Cover Observation Capacity from Civilian Earth Observation Satellites. *ISPRS J. Photogramm. Remote Sens.* **2015**, *103*, 115–128. [CrossRef]
13. Negrón-Juárez, R.I.; Holm, J.A.; Marra, D.M.; Rifai, S.W.; Riley, W.J.; Chambers, J.Q.; Koven, C.D.; Knox, R.G.; McGroddy, M.E.; Di Vittorio, A.V.; et al. Vulnerability of Amazon Forests to Storm-Driven Tree Mortality. *Environ. Res. Lett.* **2018**, *13*, 054021. [CrossRef]
14. Negrón-Juárez, R.I.; Chambers, J.Q.; Guimaraes, G.; Zeng, H.; Raupp, C.F.M.; Marra, D.M.; Ribeiro, G.H.P.M.; Saatchi, S.S.; Nelson, B.W.; Higuchi, N. Widespread Amazon Forest Tree Mortality from a Single Cross-Basin Squall Line Event. *Geophys. Res. Lett.* **2010**, *37*, L16701. [CrossRef]
15. Nelson, B.W.; Amaral, I. Destructive Wind Effects Detected in TM Images of the Amazon Basin. *Int. Arch. Photg. Rem. Sens.* **1994**, *30*, 339–343.
16. Negrón-Juárez, R.; Jenkins, H.; Raupp, C.; Riley, W.; Kueppers, L.; Magnabosco Marra, D.; Ribeiro, G.; Monteiro, M.; Candido, L.; Chambers, J.; et al. Windthrow Variability in Central Amazonia. *Atmosphere* **2017**, *8*, 28. [CrossRef]
17. Negron-Juarez, R.; Magnabosco-Marra, D.; Feng, Y.; Urquiza-Muñoz, J.D.; Riley, W.J.; Chambers, J.Q. Windthrow Characteristics and Their Regional Association with Rainfall, Soil, and Surface Elevation in the Amazon. *Environ. Res. Lett.* **2023**, *18*, 014030. [CrossRef]
18. Roy, D.P.; Wulder, M.A.; Loveland, T.R.; Woodcock, C.E.; Allen, R.G.; Anderson, M.C.; Helder, D.; Irons, J.R.; Johnson, D.M.; Kennedy, R.; et al. Landsat-8: Science and Product Vision for Terrestrial Global Change Research. *Remote Sens. Environ.* **2014**, *145*, 154–172. [CrossRef]

19. Coppin, P.; Jonckheere, I.; Nackaerts, K.; Muys, B.; Lambin, E. Digital Change Detection Methods in Ecosystem Monitoring: A Review. *Int. J. Remote Sens.* **2004**, *25*, 1565–1596. [CrossRef]
20. Goward, S.; Arvidson, T.; Williams, D.; Faundeen, J.; Irons, J.; Franks, S. Historical Record of Landsat Global Coverage: Mission Operations, NSLRSDA, and International Cooperator Stations. *Photogramm. Eng. Remote Sens.* **2006**, *72*, 1155–1169. [CrossRef]
21. Woodcock, C.E.; Strahler, A.H. The Factor of Scale in Remote Sensing. *Remote Sens. Environ.* **1987**, *21*, 311–332. [CrossRef]
22. Coops, N.C.; Wulder, M.A.; White, J.C. Identifying and Describing Forest Disturbance and Spatial Pattern: Data Selection Issues and Methodological Implications. In *Understanding Forest Disturbance and Spatial Pattern*; Wulder, M.A., Franklin, S.E., Eds.; CRC Press: Boca Raton, FL, USA, 2006; pp. 31–61.
23. Negrón-Juárez, R.I.; Chambers, J.Q.; Marra, D.M.; Ribeiro, G.H.P.M.; Rifai, S.W.; Higuchi, N.; Roberts, D. Detection of Subpixel Treefall Gaps with Landsat Imagery in Central Amazon Forests. *Remote Sens. Environ.* **2011**, *115*, 3322–3328. [CrossRef]
24. Negrón-Juárez, R.I.; Holm, J.A.; Faybishenko, B.; Magnabosco-Marra, D.; Fisher, R.A.; Shuman, J.K.; de Araujo, A.C.; Riley, W.J.; Chambers, J.Q. Landsat Near-Infrared (NIR) Band and ELM-FATES Sensitivity to Forest Disturbances and Regrowth in the Central Amazon. *Biogeosciences* **2020**, *17*, 6185–6205. [CrossRef]
25. Asner, G.P.; Kellner, J.R.; Kennedy-Bowdoin, T.; Knapp, D.E.; Anderson, C.; Martin, R.E. Forest Canopy Gap Distributions in the Southern Peruvian Amazon. *PLoS ONE* **2013**, *8*, e60875. [CrossRef] [PubMed]
26. Asner, G.P.; Keller, M.; Pereira, R., Jr.; Zweede, J.C.; Silva, J.N.M. Canopy Damage and Recovery after Selective Logging in Amazonia: Field and Satellite Studies. *Ecol. Appl.* **2004**, *14*, 280–298. [CrossRef]
27. Adams, J.B.; Gillespie, A.R. *Remote Sensing of Landscapes with Spectral Images*, 1st ed.; Adams, J.B., Gillespie, A.R., Eds.; Cambridge University Press: New York, NY, USA, 2006; ISBN 9780521662215.
28. Turner, M.G. Landscape Ecology: The Effect of Pattern on Process. *Annu. Rev. Ecol. Syst.* **1989**, *20*, 171–197. [CrossRef]
29. Wulder, M. Optical Remote-Sensing Techniques for the Assessment of Forest Inventory and Biophysical Parameters. *Prog. Phys. Geogr. Earth Environ.* **1998**, *22*, 449–476. [CrossRef]
30. Townshend, J.R.G.; Justice, C.O. Selecting the Spatial Resolution of Satellite Sensors Required for Global Monitoring of Land Transformations. *Int. J. Remote Sens.* **1988**, *9*, 187–236. [CrossRef]
31. Asner, G.P.; Warner, A.S. Canopy Shadow in IKONOS Satellite Observations of Tropical Forests and Savannas. *Remote Sens. Environ.* **2003**, *87*, 521–533. [CrossRef]
32. Clark, D.B.; Castro, C.S.; Alvarado, L.D.A.; Read, J.M. Quantifying Mortality of Tropical Rain Forest Trees Using High-Spatial-Resolution Satellite Data. *Ecol. Lett.* **2004**, *7*, 52–59. [CrossRef]
33. Clark, D.B.; Read, J.M.; Clark, M.L.; Cruz, A.M.; Dotti, M.F.; Clark, D.A. Application of 1-M and 4-M Resolution Satellite Data to Ecological Studies of Tropical Rain Forests. *Ecol. Appl.* **2004**, *14*, 61–74. [CrossRef]
34. Dalagnol, R.; Phillips, O.L.; Gloor, E.; Galvão, L.S.; Wagner, F.H.; Locks, C.J.; Aragão, L.E.O.C. Quantifying Canopy Tree Loss and Gap Recovery in Tropical Forests under Low-Intensity Logging Using VHR Satellite Imagery and Airborne LiDAR. *Remote Sens.* **2019**, *11*, 817. [CrossRef]
35. Fuller, D.O. Tropical Forest Monitoring and Remote Sensing: A New Era of Transparency in Forest Governance? *Singap. J. Trop. Geogr.* **2006**, *27*, 15–29. [CrossRef]
36. Jackson, C.; Adam, E. Remote Sensing of Selective Logging in Tropical Forests: Current State and Future Directions. *iForest-Biogeosci. For.* **2020**, *13*, 286–300. [CrossRef]
37. Espírito-Santo, F.D.B.; Keller, M.M.; Linder, E.; Oliveira Junior, R.C.; Pereira, C.; Oliveira, C.G. Gap Formation and Carbon Cycling in the Brazilian Amazon: Measurement Using High-Resolution Optical Remote Sensing and Studies in Large Forest Plots. *Plant Ecol. Divers.* **2014**, *7*, 305–318. [CrossRef]
38. Espírito-Santo, F.D.B.; Gloor, M.; Keller, M.; Malhi, Y.; Saatchi, S.; Nelson, B.; Junior, R.C.O.; Pereira, C.; Lloyd, J.; Frolking, S.; et al. Size and Frequency of Natural Forest Disturbances and the Amazon Forest Carbon Balance. *Nat. Commun.* **2014**, *5*, 3434. [CrossRef]
39. Fransson, J.E.S.; Walter, F.; Blennow, K.; Gustavsson, A.; Ulander, L.M.H. Detection of Storm-Damaged Forested Areas Using Airborne CARABAS-II VHF SAR Image Data. *IEEE Trans. Geosci. Remote Sens.* **2002**, *40*, 2170–2175. [CrossRef]
40. Dwyer, E.; Pasquali, P.; Holecz, F.; Arino, O. Mapping Forest Damage Caused by the 1999 Lothar Storm in Jura (France), Using SAR Interferometry. *Earth Obs. Q.* **2000**, *65*, 28–29.
41. Weishampel, J.F.; Drake, J.B.; Cooper, A.; Blair, J.B.; Hofton, M. Forest Canopy Recovery from the 1938 Hurricane and Subsequent Salvage Damage Measured with Airborne LiDAR. *Remote Sens. Environ.* **2007**, *109*, 142–153. [CrossRef]
42. Dalagnol, R.; Wagner, F.H.; Galvão, L.S.; Streher, A.S.; Phillips, O.L.; Gloor, E.; Pugh, T.A.M.; Ometto, J.P.H.B.; Aragão, L.E.O.C. Large-Scale Variations in the Dynamics of Amazon Forest Canopy Gaps from Airborne Lidar Data and Opportunities for Tree Mortality Estimates. *Sci. Rep.* **2021**, *11*, 1388. [CrossRef]
43. Gorgens, E.B.; Keller, M.; Jackson, T.; Marra, D.M.; Reis, C.R.; de Almeida, D.R.A.; Coomes, D.; Ometto, J.P. Out of Steady State: Tracking Canopy Gap Dynamics across Brazilian Amazon. *Biotropica* **2023**, *55*, 755–766. [CrossRef]
44. Simonetti, A.; Araújo, R.F.; Celes, C.H.; da Silva e Silva, F.R.; dos Santos, J.; Higuchi, N.; Trumbore, S.; Marra, D.M. Gap Geometry, Seasonality and Associated Losses of Biomass—Combining UAV Imagery and Field Data from a Central Amazon Forest. *Biogeosci. Discuss* 2023, *preprint*. [CrossRef]
45. Green, R.M. The Sensitivity of SAR Backscatter to Forest Windthrow Gaps. *Int. J. Remote Sens.* **1998**, *19*, 2419–2425. [CrossRef]

46. Schwarz, M.; Steinmeier, C.; Holecz, F.; Stebler, O.; Wagner, H. Detection of Windthrow in Mountainous Regions with Different Remote Sensing Data and Classification Methods. *Scand. J. For. Res.* **2003**, *18*, 525–536. [CrossRef]
47. Ping, D.; Dalagnol, R.; Galvão, L.S.; Nelson, B.; Wagner, F.; Schultz, D.M.; Bispo, P.d.C. Assessing the Magnitude of the Amazonian Forest Blowdowns and Post-Disturbance Recovery Using Landsat-8 and Time Series of PlanetScope Satellite Constellation Data. *Remote Sens.* **2023**, *15*, 3196. [CrossRef]
48. Kislov, D.E.; Korznikov, K.A. Automatic Windthrow Detection Using Very-High-Resolution Satellite Imagery and Deep Learning. *Remote Sens.* **2020**, *12*, 1145. [CrossRef]
49. Jaiswal, N.; Bucher, T.; Seiler, J.; Beckschäfer, P.; Bhattacharjee, P. Deep Learning Based Windthrow Detection for Winter Storms. In Proceedings of the Remote Sensing for Agriculture, Ecosystems, and Hydrology XXIV, Berlin, Germany, 5–7 September 2022; Neale, C.M., Maltese, A., Eds.; SPIE: Cergy, France, 2022; Volume 12262, p. 28.
50. Galizia, L.; Nasrallah, A.; Elkhoury, C.; Coutu, S.; Castet, C.; Voituron, Q. Windthrow Detection with Moderate to High Resolution Optical Imageries across the European Forests. In Proceedings of the EGU General Assembly 2023, Vienna, Austria, 24–28 April 2023. [CrossRef]
51. Deigele, W.; Brandmeier, M.; Straub, C. A Hierarchical Deep-Learning Approach for Rapid Windthrow Detection on PlanetScope and High-Resolution Aerial Image Data. *Remote Sens.* **2020**, *12*, 2121. [CrossRef]
52. Hamdi, Z.M.; Brandmeier, M.; Straub, C. Forest Damage Assessment Using Deep Learning on High Resolution Remote Sensing Data. *Remote Sens.* **2019**, *11*, 1976. [CrossRef]
53. Kislov, D.E.; Korznikov, K.A.; Altman, J.; Vozmishcheva, A.S.; Krestov, P. V Extending Deep Learning Approaches for Forest Disturbance Segmentation on Very High-resolution Satellite Images. *Remote Sens. Ecol. Conserv.* **2021**, *7*, 355–368. [CrossRef]
54. Andreae, M.O.; Acevedo, O.C.; Araùjo, A.; Artaxo, P.; Barbosa, C.G.G.; Barbosa, H.M.J.; Brito, J.; Carbone, S.; Chi, X.; Cintra, B.B.L.; et al. The Amazon Tall Tower Observatory (ATTO): Overview of Pilot Measurements on Ecosystem Ecology, Meteorology, Trace Gases, and Aerosols. *Atmos. Chem. Phys.* **2015**, *15*, 10723–10776. [CrossRef]
55. Stropp, J.; Van der Sleen, P.; Assunção, P.A.; da Silva, A.L.; Ter Steege, H. Tree Communities of White-Sand and Terra-Firme Forests of the Upper Rio Negro. *Acta Amaz.* **2011**, *41*, 521–544. [CrossRef]
56. Targhetta, N.; Kesselmeier, J.; Wittmann, F. Effects of the Hydroedaphic Gradient on Tree Species Composition and Aboveground Wood Biomass of Oligotrophic Forest Ecosystems in the Central Amazon Basin. *Folia Geobot* **2015**, *50*, 185–205. [CrossRef]
57. De Oliveira, A.N.; Amaral, I.L. do Florística e Fitossociologia de Uma Floresta de Vertente Na Amazônia Central, Amazonas, Brasil. *Acta Amaz.* **2004**, *34*, 21–34. [CrossRef]
58. Braga, P.I.S. Subdivisão Fitogeográfica, Tipos de Vegetação, Conservação e Inventário Florístico Da Floresta Amazônica. *Acta Amaz.* **1979**, *9*, 53–80. [CrossRef]
59. Higuchi, N.; Chambers, J.; Santos, J. Dos Dinâmica e Balanço Do Carbono Da Vegetação Primária Da Amazônia Central. *Floresta* **2004**, *34*, 295–304. [CrossRef]
60. Telles, E.d.C.C.; de Camargo, P.B.; Martinelli, L.A.; Trumbore, S.E.; da Costa, E.S.; Santos, J.; Higuchi, N.; Oliveira, R.C. Influence of Soil Texture on Carbon Dynamics and Storage Potential in Tropical Forest Soils of Amazonia. *Glob. Biogeochem. Cycles* **2003**, *17*, 1040. [CrossRef]
61. Carneiro, V.M.C. *Composição Florística e Análise Estrutural Da Floresta Primária de Terra Firme Na Bacia Do Rio Cuieiras*; Universidade Federal do Amazonas: Manaus, Brazil, 2004.
62. Chambers, J.Q.; Robertson, A.L.; Carneiro, V.M.C.; Lima, A.J.N.; Smith, M.-L.; Plourde, L.C.; Higuchi, N. Hyperspectral Remote Detection of Niche Partitioning among Canopy Trees Driven by Blowdown Gap Disturbances in the Central Amazon. *Oecologia* **2009**, *160*, 107–117. [CrossRef]
63. Pinto, A.C.; Higuchi, N.; Iida, S.; Santos, J.; Ribeiro, R.J.; Rocha, R.M.; Silva, R.P. Padrão de Distribuição Espacial de Espécies Florestais Que Ocorrem Na Região de Manaus. In *Projeto Jacaranda Fase II—Pesquisas Florestais na Amazônia Central*; Higuchi, N., Santos, J., Sampaio, P.T., Marenco, R.A., Ferraz, J., Sales, P.C., Saito, M., Matsumoto, S., Eds.; National Institute of Amazon Research: Manaus, Brazil, 2003; pp. 1–20.
64. Anderson, A.B. White-Sand Vegetation of Brazilian Amazonia. *Biotropica* **1981**, *13*, 199. [CrossRef]
65. Adeney, J.M.; Christensen, N.L.; Vicentini, A.; Cohn-Haft, M. White-sand Ecosystems in Amazonia. *Biotropica* **2016**, *48*, 7–23. [CrossRef]
66. Luizão, F.J.; Schubart, H.O.R. Litter Production and Decomposition in a Terra-Firme Forest of Central Amazonia. *Experientia* **1987**, *43*, 259–265. [CrossRef]
67. Ferraz, J.; Ohta, S.; de Sales, P.C. Distribuição Dos Solos Ao Longo de Dois Transectos Em Floresta Primária Ao Norte de Manaus (AM). In *Pesquisas Florestais Para a Conservação da Floresta e Reabilitação de Áreas Degradadas da Amazônia*; MCT-INPA/JICA, Ed.; INPA: Manaus, Brazil, 1998; pp. 109–143.
68. De Almeida, A.F. Análise Fitossociológica Estrutural e Composição Florística da Área de Proteção Ambiental Margem Esquerda do Rio Negro. Master's Thesis, Universidade Federal do Amazonas, Manaus, Brazil, 2012.
69. Amaral, I.L.D.; Matos, F.D.A.; Lima, J. Composição Florística e Parâmetros Estruturais de Um Hectare de Floresta Densa de Terra Firme No Rio Uatumã, Amazônia, Brasil. *Acta Amaz.* **2000**, *30*, 377. [CrossRef]
70. Woortmann, C.P.; Higuchi, N.; Dos Santos, J.; Da Silva, R.P. Allometric Equations for Total, above-and below-Ground Biomass and Carbon of the Amazonian Forest Type Known as Campinarana. *Acta Amaz.* **2018**, *48*, 85–92. [CrossRef]

71. Gorelick, N.; Hancher, M.; Dixon, M.; Ilyushchenko, S.; Thau, D.; Moore, R. Google Earth Engine: Planetary-Scale Geospatial Analysis for Everyone. *Remote Sens. Environ.* **2017**, *202*, 18–27. [CrossRef]
72. Adams, J.B.; Sabol, D.E.; Kapos, V.; Almeida Filho, R.; Roberts, D.A.; Smith, M.O.; Gillespie, A.R. Classification of Multispectral Images Based on Fractions of Endmembers: Application to Land-Cover Change in the Brazilian Amazon. *Remote Sens. Environ.* **1995**, *52*, 137–154. [CrossRef]
73. Shimabukuro, Y.E.; Smith, J.A. The Least-Squares Mixing Models to Generate Fraction Images Derived from Remote Sensing Multispectral Data. *IEEE Trans. Geosci. Remote Sens.* **1991**, *29*, 16–20. [CrossRef]
74. Ponzoni, F.J.; Shimabukuro, Y.E.; Kuplich, T.M. (Eds.) *Sensoriamento Remoto No Estudo Da Vegetação*, 2nd ed.; Oficina de Textos: São Paulo, Brazil, 2012; ISBN 978-85-7975-053-3.
75. Somers, B.; Asner, G.P.; Tits, L.; Coppin, P. Endmember Variability in Spectral Mixture Analysis: A Review. *Remote Sens. Environ.* **2011**, *115*, 1603–1616. [CrossRef]
76. *Environment for Visualizing Images: ENVI 5.3*; Exelis Visual Solutions Information: Boulder, CO, USA, 2010.
77. Green, A.A.; Berman, M.; Switzer, P.; Craig, M.D. A Transformation for Ordering Multispectral Data in Terms of Image Quality with Implications for Noise Removal. *IEEE Trans. Geosci. Remote Sens.* **1988**, *26*, 65–74. [CrossRef]
78. Shimabukuro, Y.E.; Ponzoni, F.J. *Mistura Espectral: Modelo Linear e Aplicações*; Yosio Edemir Shimabukuro, F.J.P., Ed.; Oficina de Textos: São Paulo, Brasil, 2017; ISBN 978-85-7975-270-4.
79. NV5. *Environment for Visualizing Images*; Geospatial ENVI: Broomfield, CO, USA, 2023.
80. Uptike, T.; Comp, C. Radiometric Use of WorldView-2 Imagery. Available online: https://dg-cms-uploads-production.s3.amazonaws.com/uploads/document/file/104/Radiometric_Use_of_WorldView-2_Imagery.pdf (accessed on 11 May 2022).
81. L3HARRIS Linear Spectral Unmixing. Available online: https://www.l3harrisgeospatial.com/docs/linearspectralunmixing.html (accessed on 19 January 2022).
82. Nelson, B.W.; Kapos, V.; Adams, J.B.; Oliveira, W.J.; Braun, O.P.G.G. Forest Disturbance by Large Blowdowns in the Brazilian Amazon. *Ecology* **1994**, *75*, 853–858. [CrossRef]
83. Roberts, D.A.; Smith, M.O.; Adams, J.B. Green Vegetation, Nonphotosynthetic Vegetation, and Soils in AVIRIS Data. *Remote Sens. Environ.* **1993**, *44*, 255–269. [CrossRef]
84. Adams, J.B.; Smith, M.O.; Gillespie, A.R. Imaging Spectroscopy: Interpretation Based on Spectral Mixture Analysis. In *Remote Geochemical Analysis: Elemental and Mineralogical Composition*; Pieters, V.M., Englert, P., Eds.; Cambridge University Press: New York, NY, USA, 1993; pp. 145–166.
85. Souza, C.M.; Roberts, D.A.; Cochrane, M.A. Combining Spectral and Spatial Information to Map Canopy Damage from Selective Logging and Forest Fires. *Remote Sens. Environ.* **2005**, *98*, 329–343. [CrossRef]
86. Chambers, J.Q.; Asner, G.P.; Morton, D.C.; Anderson, L.O.; Saatchi, S.S.; Espírito-Santo, F.D.B.; Palace, M.; Souza, C. Regional Ecosystem Structure and Function: Ecological Insights from Remote Sensing of Tropical Forests. *Trends Ecol. Evol.* **2007**, *22*, 414–423. [CrossRef] [PubMed]
87. QGIS Development Team. *QGIS Geographic Information System*; Open Source Geospatial Foundation Project: Beaverton, OR, USA, 2016.
88. McCullagh, P.; Nelder, J.A. *Generalized Linear Models*, 2nd ed.; McCullagh, P., Nelder, J.A., Eds.; Taylor & Francis Group: Boca Raton, FL, USA, 1989; ISBN 0-412-31760-5.
89. Hawkins, D.M. The Problem of Overfitting. *J. Chem. Inf. Comput. Sci.* **2004**, *44*, 1–12. [CrossRef]
90. Murtaugh, P.A. In Defense of P Values. *Ecology* **2014**, *95*, 611–617. [CrossRef] [PubMed]
91. Kullback, S. *Information Theory and Statistics*; Wiley, Ed.; Dover Publications: New York, NY, USA, 1997; ISBN 0-486-69684-7.
92. Cameron, A.C.; Windmeijer, F.A.G. An R-Squared Measure of Goodness of Fit for Some Common Nonlinear Regression Models. *J. Econom.* **1997**, *77*, 329–342. [CrossRef]
93. Gotelli, N.J.; Ellinson, A.M. *A Primer of Ecological Statistics*, 2nd ed.; Sinauer Associates: Sunderland, MA, USA, 2013; ISBN 9781605350646.
94. Smith, T.J.; McKenna, C.M. A Comparison of Logistic Regression Pseudo R 2 Indices. *Mult. Linear Regres. Viewp.* **2013**, *39*, 17–26.
95. Sheskin, D.J. *Handbook of Parametric and Nonparametric Statistical Procedures*, 3rd ed.; Chapman and Hall/CRC, Ed.; Chapman and Hall/CRC: New York, NY, USA, 2003; ISBN 9780429186165.
96. Le Cam, L. The Central Limit Theorem around 1935. *Stat. Sci.* **1986**, *1*, 78–91.
97. R Core Team. *R: A Language and Environment for Statistical Computing*; R Foundation for Statistical Computing: Vienna, Austria, 2022.
98. Goel, N.S.; Strebel, D.E.; Thompson, R.L. Inversion of Vegetation Canopy Reflectance Models for Estimating Agronomic Variables. II. Use of Angle Transforms and Error Analysis as Illustrated by Suits' Model. *Remote Sens. Environ.* **1984**, *14*, 77–111. [CrossRef]
99. Asner, G.P.; Palace, M.; Keller, M.; Pereira, R.; Silva, J.N.M.; Zweede, J.C. Estimating Canopy Structure in an Amazon Forest from Laser Range Finder and IKONOS Satellite Observations. *Biotropica* **2002**, *34*, 483–492. [CrossRef]
100. Theiler, J.; Ziemann, A.; Matteoli, S.; Diani, M. Spectral Variability of Remotely Sensed Target Materials: Causes, Models, and Strategies for Mitigation and Robust Exploitation. *IEEE Geosci. Remote Sens. Mag.* **2019**, *7*, 8–30. [CrossRef]
101. Peterson, C.J.; Ribeiro, G.; Negrón-Juárez, R.; Marra, D.M.; Chambers, J.Q.; Higuchi, N.; Lima, A.; Cannon, J.B. Critical Wind Speeds Suggest Wind Could Be an Important Disturbance Agent in Amazonian Forests. *For. Int. J. For. Res.* **2019**, *92*, 444–459. [CrossRef]

102. Ribeiro, G.H.P.M.; Chambers, J.Q.; Peterson, C.J.; Trumbore, S.E.; Magnabosco Marra, D.; Wirth, C.; Cannon, J.B.; Négron-Juárez, R.I.; Lima, A.J.N.; de Paula, E.V.C.M.; et al. Mechanical Vulnerability and Resistance to Snapping and Uprooting for Central Amazon Tree Species. *For. Ecol. Manag.* **2016**, *380*, 1–10. [CrossRef]
103. Strahler, A.H.; Woodcock, C.E.; Smith, J.A. On the Nature of Models in Remote Sensing. *Remote Sens. Environ.* **1986**, *20*, 121–139. [CrossRef]
104. Dos Santos, L.T.; Marra, D.M.; Trumbore, S.; De Camargo, P.B.; Negrón-Juárez, R.I.; Lima, A.J.N.; Ribeiro, G.H.P.M.; Dos Santos, J.; Higuchi, N. Windthrows Increase Soil Carbon Stocks in a Central Amazon Forest. *Biogeosciences* **2016**, *13*, 1299–1308. [CrossRef]
105. Viljur, M.; Abella, S.R.; Adámek, M.; Alencar, J.B.R.; Barber, N.A.; Beudert, B.; Burkle, L.A.; Cagnolo, L.; Campos, B.R.; Chao, A.; et al. The Effect of Natural Disturbances on Forest Biodiversity: An Ecological Synthesis. *Biol. Rev.* **2022**, *97*, 1930–1947. [CrossRef] [PubMed]
106. Alencar, J.B.R.; da Fonseca, C.R.V.; Marra, D.M.; Baccaro, F.B. Windthrows Promote Higher Diversity of Saproxylic Beetles (Coleoptera: Passalidae) in a Central Amazon Forest. *Insect Conserv. Divers.* **2022**, *15*, 1–8. [CrossRef]
107. Espirito-Santo, F.D.B.; Saatchi, S.; Keller, M. Detecting Tree-Fall Gap Disturbances in Tropical Rain Forests with Airborne Lidar. *AGUFM* **2017**, *2017*, B14C-01.
108. Silvério, D.V.; Brando, P.M.; Bustamante, M.M.C.; Putz, F.E.; Marra, D.M.; Levick, S.R.; Trumbore, S.E. Fire, Fragmentation, and Windstorms: A Recipe for Tropical Forest Degradation. *J. Ecol.* **2019**, *107*, 656–667. [CrossRef]
109. Planet Team. Available online: https://www.planet.com/products/ (accessed on 22 April 2022).
110. Dial, G.; Bowen, H.; Gerlach, F.; Grodecki, J.; Oleszczuk, R. IKONOS Satellite, Imagery, and Products. *Remote Sens. Environ.* **2003**, *88*, 23–36. [CrossRef]
111. Toutin, T. Review Article: Geometric Processing of Remote Sensing Images: Models, Algorithms and Methods. *Int. J. Remote Sens.* **2004**, *25*, 1893–1924. [CrossRef]
112. Loveland, T.R.; Dwyer, J.L. Landsat: Building a Strong Future. *Remote Sens. Environ.* **2012**, *122*, 22–29.
113. Storey, J.; Roy, D.P.; Masek, J.; Gascon, F.; Dwyer, J.; Choate, M. A Note on the Temporary Misregistration of Landsat-8 Operational Land Imager (OLI) and Sentinel-2 Multi Spectral Instrument (MSI) Imagery. *Remote Sens. Environ.* **2016**, *186*, 121–122. [CrossRef]
114. Trémas, T.L.; Déchoz, C.; Lacherade, S.; Nosavan, J.; Petrucci, B. Sentinel-2: Presentation of the CAL/VAL Commissioning Phase. *Image Signal Process. Remote Sens. XXI* **2015**, *9643*, 94–106. [CrossRef]
115. DigitalGlobe WorldView 2. Available online: http://www.engesat.com.br/imagem-de-satelite/world-view-2/ (accessed on 28 February 2021).
116. Hand, D.J. *Statistics: A Very Short Introduction*, 1st ed.; Oxford University Press: New York, NY, USA, 2008; ISBN 9780199233564.
117. Galvão, L.S.; dos Santos, J.R.; Roberts, D.A.; Breunig, F.M.; Toomey, M.; de Moura, Y.M. On Intra-Annual EVI Variability in the Dry Season of Tropical Forest: A Case Study with MODIS and Hyperspectral Data. *Remote Sens. Environ.* **2011**, *115*, 2350–2359. [CrossRef]
118. Clark, M.L.; Roberts, D.A.; Clark, D.B. Hyperspectral Discrimination of Tropical Rain Forest Tree Species at Leaf to Crown Scales. *Remote Sens. Environ.* **2005**, *96*, 375–398. [CrossRef]
119. Muller-Karger, F.E.; Hestir, E.; Ade, C.; Turpie, K.; Roberts, D.A.; Siegel, D.; Miller, R.J.; Humm, D.; Izenberg, N.; Keller, M.; et al. Satellite Sensor Requirements for Monitoring Essential Biodiversity Variables of Coastal Ecosystems. *Ecol. Appl.* **2018**, *28*, 749–760. [CrossRef]
120. Denslow, J. Tropical Rainforest Gaps And Tree Species Diversity. *Annu. Rev. Ecol. Syst.* **1987**, *18*, 431–451. [CrossRef]
121. Vitousek, P.M.; Denslow, J.S. Nitrogen and Phosphorus Availability in Treefall Gaps of a Lowland Tropical Rainforest. *J. Ecol.* **1986**, *74*, 1167. [CrossRef]
122. USGS Landsat Science. Available online: https://landsat.gsfc.nasa.gov/satellites/landsat-8/ (accessed on 4 August 2022).
123. European Space Agency. SENTINEL-2 User Handbook. Available online: https://sentinels.copernicus.eu/documents/247904/685211/Sentinel-2_User_Handbook.pdf/8869acdf-fd84-43ec-ae8c-3e80a436a16c?t=1438278087000 (accessed on 22 April 2021).
124. European Space Agency. Sentinel 2 Level 2A. Available online: https://sentinel.https//sentinel.esa.int/web/sentinel/user-guides/sentinel-2-msi (accessed on 28 June 2021).
125. Martins, V.S.; Novo, E.M.L.M.; Lyapustin, A.; Aragão, L.E.O.C.; Freitas, S.R.; Barbosa, C.C.F. Seasonal and Interannual Assessment of Cloud Cover and Atmospheric Constituents across the Amazon (2000–2015): Insights for Remote Sensing and Climate Analysis. *ISPRS J. Photogramm. Remote Sens.* **2018**, *145*, 309–327. [CrossRef]
126. Williams, D.L.; Goward, S.; Arvidson, T. Landsat: Yesterday, Today, and Tomorrow. *Photogramm. Eng. Remote Sens.* **2006**, *72*, 1171–1178.
127. Norway's International Climate and Forest Initiative. Available online: https://www.nicfi.no/ (accessed on 22 April 2023).
128. Roy, D.P.; Huang, H.; Houborg, R.; Martins, V.S. A Global Analysis of the Temporal Availability of PlanetScope High Spatial Resolution Multi-Spectral Imagery. *Remote Sens. Environ.* **2021**, *264*, 112586. [CrossRef]